

Photolysis of methyl nitrate (CH_3ONO_2) through the prism of *ab initio* simulations of transient-absorption pump-probe spectra

Cite as: J. Chem. Phys. 162, 224302 (2025); doi: 10.1063/5.0256037

Submitted: 2 January 2025 • Accepted: 1 May 2025 •

Published Online: 10 June 2025



View Online



Export Citation



CrossMark

Juanjuan Zhang,¹ Deping Hu,² Jiawei Peng,¹ Maxim F. Gelin,^{3,a)} and Zhenggang Lan^{1,a)}

AFFILIATIONS

¹ SCNU Environmental Research Institute, Guangdong Provincial Key Laboratory of Chemical Pollution and Environmental Safety and MOE Key Laboratory of Environmental Theoretical Chemistry, School of Environment, South China Normal University, Guangzhou 510006, China

² Center for Advanced Materials Research, Beijing Normal University, Zhuhai 519087, China

³ School of Science, Hangzhou Dianzi University, Hangzhou 310018, China

^{a)} Authors to whom correspondence should be addressed: maxim@hdu.edu.cn and zhenggang.lan@m.scnu.edu.cn

ABSTRACT

The photolysis of methyl nitrate (CH_3ONO_2) UV-excited to the optically bright state is scrutinized by on-the-fly trajectory surface hopping simulations of dynamic observables and transient-absorption pump-probe (TA-PP) spectra. It is found that two major dissociation channels, $\text{CH}_3\text{O} + \text{NO}_2$ and $\text{CH}_3\text{O} + \text{NO} + \text{O}$, are characterized by the two branches of the stimulated emission signal, which are clearly seen in the total experimentally detectable TA-PP signal. Correlations between the photolysis channels and their TA-PP signatures are established. It is argued that TA-PP spectra may provide valuable information on the multi-channel photolysis mechanisms in similar compounds, and combining *ab initio* simulations of the dynamic and spectroscopic observables may enhance our understanding of the photodissociation mechanisms and pathways.

Published under an exclusive license by AIP Publishing. <https://doi.org/10.1063/5.0256037>

I. INTRODUCTION

Volatile organic compounds (VOCs) are well-known atmospheric pollutants that play an essential role in the global warming and formation of harmful particulate matters.^{1–20} Among them, alkyl nitrates received great research attention, because their photolysis products NO_x after UV radiation cause significant environmental impacts on the air quality and nutrient cycle.^{21–26} Many experimental and theoretical studies focused on methyl nitrate (CH_3ONO_2 , the simplest alkyl nitrate) and its derivatives to clarify the key mechanisms in the photoinduced reaction.^{23–25,27–43}

In experimental studies, the absorption spectra and photolysis products of CH_3ONO_2 were measured.^{22–25,28,30,35,38,44} As its photoproducts show significant diversity and their ratios highly depend on the excitation wavelengths,^{22,23,25,28,30,35,38,45} the detection of these photoproducts is not a trivial task. On the theoretical side, the reaction pathways were constructed and the photolysis dynamics were simulated.^{34,40,41,45} However, the accurate theoretical description of

such a system is still quite challenging, because the excited-state reaction of CH_3ONO_2 involves several coupled electronic states and the state degeneracy exists in the dissociation limit.^{34,40} At the same time, the precise understanding requires the very accurate description on the molecular excited states. However, this is also a very challenging task, even for small compounds.

After many experimental and theoretical studies on CH_3ONO_2 ,^{22–25,34–36,38–40} a fairly good understanding of the basic features for its photolysis was established. First, the UV absorption spectrum of CH_3ONO_2 includes two bands. A weak broad shoulder-type band around 240–330 nm corresponds to the electronic transitions to the two lowest excited states S_1 and S_2 with low oscillator strengths.^{34,35,38,40} A strong band around 190 nm reveals transitions to the higher bright states.^{23,25,40} Second, the photolysis channels of CH_3ONO_2 depend significantly on the UV excitation wavelength. Both experimental and theoretical studies agree that in the low energy domain, channel-I ($\text{CH}_3\text{O} + \text{NO}_2$) dominates.^{25,34,38,40} In addition, the theoretical simulations

suggested that the internal conversion to the ground state takes place earlier than the dissociation.^{34,40,41} At the higher excitation energy domain, other photolysis channels such as channel-II ($\text{CH}_3\text{O} + \text{NO} + \text{O}$) and channel-III ($\text{CH}_3\text{ONO} + \text{O}$) become important.^{25,34,40} The energy released in the photolysis dynamics mainly flows to the NO_2 moiety, instead of the CH_3O part. Third, some molecular vibrational modes, such as the $\text{CH}_3\text{O}-\text{NO}_2$ bond stretching and the bending motion of $\text{O}-\text{N}-\text{O}$ in the NO_2 moiety, are rather critical in the photolysis dynamics.⁴⁰ The mode-specific excitation of these motions may bring an important impact on the excited-state nonadiabatic dynamics of CH_3ONO_2 .⁴⁵

Analyzing the entire body of the available data on the photoinduced processes in CH_3ONO_2 (and, parenthetically, in other molecular systems), one notices a clear imbalance between theoretical and experimental studies. Theoreticians prefer to calculate/simulate “theoretical quantities,” that is, evolutions of populations, bond angles, bond lengths, etc., in different electronic states. These theoretical quantities, however, cannot be directly detected, because experimentalists measure spectra and time-resolved spectroscopic signals that cannot be reduced to the aforementioned theoretical observables. The aim of this work is to uncover correlations between theoretical and experimental observables, to study what we can learn from these observables on the photoinduced dynamics in CH_3ONO_2 , and to explore how the theoretical observables can facilitate and enhance the interpretation of the experimental observables. In fact, the direct simulation of experimental observables is a long-lasting research topic in the field of photoinduced ultrafast dynamics.^{46–55}

As the CH_3ONO_2 photolysis takes place on the femtosecond timescale, we choose to simulate femtosecond transient-absorption pump-probe (TA-PP) spectra as experimental observables. Our choice is substantiated by the fact that TA-PP spectroscopy is, perhaps, the most common nonlinear technique intended for the exploration of the nonadiabatic dynamics of various molecular systems.^{56–68}

Pollard, Lee, and Mathies gave a wavefunction-based perturbation theory of TA-PP spectra.^{69,70} The general quantum framework of TA-PP spectroscopy was developed by Mukamel and co-workers in terms of third-order response functions.^{56–68} Under the assumption that the pump and probe pulses do not overlap, Yan, Fried, and Mukamel proposed the doorway-window (DW) picture of the TA-PP signals, at both quantum and classical levels of description.^{71,72} The classical representations of TA-PP spectra were also elaborated by Stock,⁷³ Martens and co-workers,⁷⁴ Cina and co-workers,⁷⁵ and Loring and co-workers.^{76,77} These earlier studies laid theoretical foundations for the *ab initio* simulations of nonlinear femtosecond spectroscopic responses. In recent years, significant theoretical efforts were devoted to simulating TA-PP signals within the framework of the on-the-fly nonadiabatic dynamics,^{63,78–89} as these approaches allow us to obtain time-resolved signals of realistic molecular systems that may experience large-amplitude or arbitrary nuclear motions. The bulk majority of these approaches are based on the (quasi)classical evaluation of the nonlinear response functions.^{63,78–89} Yet, the TA-PP spectra of molecular chromophores were also computed with the spectroscopic equation-of-motion approach⁶⁹ through the on-the-fly propagation of time-dependent system pulsing field Hamiltonians.^{81,83,90–92}

Among the developed methods, the classical DW approximation allows us to efficiently compute the nonlinear spectroscopic signals.^{72,81,86–88} The combination of the DW methodology and on-the-fly trajectory surface hopping (TSH) nonadiabatic dynamics provides a useful framework (TSH-DW) to simulate TA-PP signals. In fact, this approach displays a powerful ability to balance the efficiency and accuracy in the simulations of different ultrafast time-resolved signals, including TA-PP, time-resolved fluorescence, and two-dimensional electronic spectra.^{86–88,93–97}

In this work, we employ the TSH-DW protocol to simulate the TA-PP spectra of CH_3ONO_2 . The remainder of this paper is structured as follows. Section II contains the appropriate technical details on the TSH-DW simulations. The results of the simulations are presented and discussed in Sec. III, which consists of three parts. In Sec. III A, we give a brief recapitulation of the main theoretical observables. The reader who is familiar with (or uninterested in) the matter can proceed directly to Sec. III B, in which we attempt to interpret the simulated TA-PP spectra and extract the characteristic timescales without using preknowledge on the nonadiabatic dynamics of CH_3ONO_2 . In Sec. III C, we invoke the theoretical observables of Sec. III A for a more detailed characterization of the ultrafast CH_3ONO_2 photolysis. Section IV concludes our work.

II. COMPUTATIONAL DETAILS

The TA-PP spectra of CH_3ONO_2 were simulated within the framework of the nonlinear response functions using the TSH-DW approximation. As the details of the DW representation of the TA-PP signals can be found in previous studies,^{72,87,88,93,94} we only discuss the main ideas here.

The TSH-DW protocol requires two groups of dynamics simulations, the TSH dynamics in the coupled excited electronic states, and the ground state Born–Oppenheimer molecular dynamics (BOMD). The TSH dynamics is used to describe the nonadiabatic dynamics after photoexcitation. Following the previous work,^{40,45} we ran the TSH dynamics at the XMS-CASPT2 level^{98–100} using our JADE-NAMD code.^{101–103} All simulation details are very similar to those in our previous work,⁴⁰ and we thus give them in the *supplementary material*. We mention just two differences with Ref. 40: (i) more trajectories (200) were simulated to get more accurate correlations between the nonadiabatic dynamics and TA-PP signals, and (ii) in TA-PP simulations, the ground state BOMD describes the hole motion initialized by the pump pulse. Starting from the same initial conditions, the BOMD was simulated at the B3LYP/def2-SVP level with the D3-(BJ) dispersion correction.¹⁰⁴ Along the trajectory propagation, molecular coordinates, energies of excited states, and transition dipole moments (TDMs) between different electronic states were obtained in both BOMD and TSH dynamics.

The total integrated TA-PP signal $I_{\text{int}}(\tau, \omega_{pr})$ is usually monitored as a function of the time delay τ between the pump and probe pulses and the probe-pulse frequency ω_{pr} (see, e.g., Ref. 69). The signal consists of three contributions, i.e., stimulated emission (SE) $I_{\text{int}}^{\text{SE}}(\tau, \omega_{pr})$, excited-state absorption (ESA) $I_{\text{int}}^{\text{ESA}}(\tau, \omega_{pr})$, and ground-state bleach (GSB) $I_{\text{int}}^{\text{GSB}}(\tau, \omega_{pr})$. When the pump and probe pulses are well temporally separated and their durations are much shorter than the characteristic timescale of the system evolution, it is

possible to employ the DW approximation to compute TA-PP signals as follows:^{87,93,94}

$$I_{\text{int}}(\tau, \omega_{pr}) = I_{\text{int}}^{\text{GSB}}(\tau, \omega_{pr}) + I_{\text{int}}^{\text{SE}}(\tau, \omega_{pr}) + I_{\text{int}}^{\text{ESA}}(\tau, \omega_{pr}), \quad (1)$$

$$\begin{aligned} I_{\text{int}}^{\text{GSB}}(\tau, \omega_{pr}) &= \omega_{pr} \int d\mathbf{R}_g d\mathbf{P}_g D_0(\omega_{pu}, \mathbf{R}_g, \mathbf{P}_g) \\ &\times W_0^{\text{int}}(\omega_{pr}, \mathbf{R}_g(\tau), \mathbf{P}_g(\tau)), \end{aligned} \quad (2)$$

$$\begin{aligned} I_{\text{int}}^{\text{SE}}(\tau, \omega_{pr}) &= \omega_{pr} \int d\mathbf{R}_g d\mathbf{P}_g D_I(\omega_{pu}, \mathbf{R}_g, \mathbf{P}_g) \\ &\times W_I^{\text{int}}(\omega_{pr}, \mathbf{R}_e(\tau), \mathbf{P}_e(\tau)), \end{aligned} \quad (3)$$

$$\begin{aligned} I_{\text{int}}^{\text{ESA}}(\tau, \omega_{pr}) &= -\omega_{pr} \int d\mathbf{R}_g d\mathbf{P}_g D_I(\omega_{pu}, \mathbf{R}_g, \mathbf{P}_g) \\ &\times W_{II}^{\text{int}}(\omega_{pr}, \mathbf{R}_e(\tau), \mathbf{P}_e(\tau)). \end{aligned} \quad (4)$$

Here, \mathbf{R}_g and \mathbf{P}_g are the initial nuclear coordinates and momenta that are sampled from the Wigner distribution $\rho_g^{\text{Wig}}(\mathbf{R}_g, \mathbf{P}_g)$. $\mathbf{R}_g(\tau)$ and $\mathbf{P}_g(\tau)$ are the nuclear coordinates and momenta propagated in the electronic ground state up to $t = \tau$. $\mathbf{R}_e(\tau)$ and $\mathbf{P}_e(\tau)$ are the nuclear coordinates and momenta that are nonadiabatically propagated on an electronic excited state $e(t)$ up to $t = \tau$. The explicit expressions for the doorway (D_0, D_I) and window (W_0, W_I , and W_{II}) functions are given as follows:

$$D_0(\omega_{pu}, \mathbf{R}_g, \mathbf{P}_g) = \sum_e \left| \epsilon_{pu} \boldsymbol{\mu}_{ge}(\mathbf{R}_g) \right|^2 E_{pu}^2 [\omega_{pu} - U_{eg}(\mathbf{R}_g)] \rho_g^{\text{Wig}}(\mathbf{R}_g, \mathbf{P}_g), \quad (5)$$

$$D_I(\omega_{pu}, \mathbf{R}_g, \mathbf{P}_g) = \left| \epsilon_{pu} \boldsymbol{\mu}_{ge}(\mathbf{R}_g) \right|^2 E_{pu}^2 [\omega_{pu} - U_{eg}(\mathbf{R}_g)] \rho_g^{\text{Wig}}(\mathbf{R}_g, \mathbf{P}_g), \quad (6)$$

$$\begin{aligned} W_0^{\text{int}}(\omega_{pr}, \mathbf{R}_g(\tau), \mathbf{P}_g(\tau)) &= \sum_e \left| \epsilon_{pr} \boldsymbol{\mu}_{ge}(\mathbf{R}_g(\tau)) \right|^2 \\ &\times E_{pr}^2 [\omega_{pr} - U_{eg}(\mathbf{R}_g(\tau))], \end{aligned} \quad (7)$$

$$\begin{aligned} W_I^{\text{int}}(\omega_{pr}, \mathbf{R}_e(\tau), \mathbf{P}_e(\tau)) &= \left| \epsilon_{pr} \boldsymbol{\mu}_{ge(\tau)}(\mathbf{R}_e(\tau)) \right|^2 \\ &\times E_{pr}^2 [\omega_{pr} - U_{e(\tau)g}(\mathbf{R}_e(\tau))], \end{aligned} \quad (8)$$

$$\begin{aligned} W_{II}^{\text{int}}(\omega_{pr}, \mathbf{R}_e(\tau), \mathbf{P}_e(\tau)) &= \sum_f \left| \epsilon_{pr} \boldsymbol{\mu}_{e(\tau)f}(\mathbf{R}_e(\tau)) \right|^2 \\ &\times E_{pr}^2 [\omega_{pr} - U_{fe(\tau)}(\mathbf{R}_e(\tau))]. \end{aligned} \quad (9)$$

Here, $E_{pu}(\omega)$ and $E_{pr}(\omega)$ are the Fourier transforms of the dimensionless envelopes $E_{pu}(t)$ and $E_{pr}(t)$ of the pump and probe pulses, respectively; the ground and excited electronic states are denoted as g and e , respectively; $\boldsymbol{\mu}_{ge}[\mathbf{R}_g(\tau)]$, $\boldsymbol{\mu}_{ge}[\mathbf{R}_e(\tau)]$, and $\boldsymbol{\mu}_{e(\tau)f}[\mathbf{R}_e(\tau)]$ are the TDMs for a specific nuclear configuration $\mathbf{R}_g(\tau)$ or $\mathbf{R}_e(\tau)$; and $U_{eg}[\mathbf{R}_g(\tau)]$, $U_{e(\tau)g}[\mathbf{R}_e(\tau)]$, and $U_{fe(\tau)}[\mathbf{R}_e(\tau)]$ are the energy gaps between the corresponding electronic states. The meaning of $e(\tau)$ is that a trajectory initiated at $t = 0$ in a state e can end up at time $t = \tau$ in another state or in the ground state. When the internal

conversion to the ground state takes place, we need to slightly modify the above expressions to compute the window function for the trajectory staying on the excited state or going back to the ground state. All trajectories were taken into account for the spectral calculations. More details can be found in our previous work.⁹³

It is essential to clarify that the doorway functions are specified by the TDMs and transition frequencies at $\tau = 0$, as well as by the carrier frequency ω_{pu} and envelope of the pump pulse. The window functions, on the other hand, are determined by the TDMs and transition frequencies evaluated at a time τ along the trajectory in the electronic ground state (W_0) and in the low-lying excited electronic states (W_I , W_{II}), as well as by the carrier frequency ω_{pr} and envelope of the probe pulse.

The GSB signal is represented by a sum of the so-called hot and cold signals. The hot GSB signal is determined by the wavepackets that arrive in the electronic ground-state owing to the internal conversion from the excited states. Along the “hot” trajectory on the ground state, after it hops from S_1 , we calculate the excitation energies of the low-lying excited states and their TDMs. By considering them and the probe laser field, we obtain the hot window function $-W_0$. After combining the doorway function D_I and the hot window function $-W_0$, the hot GSB signal is evaluated. The cold GSB signal is a conventional GSB signal, which reveals the motion of the “hole” created by the pump laser. As a consequence, the doorway function D_0 is governed by the electronic transitions to all low-lying excited states involved in the excitation by the pump laser pulse. Thus, the expression for D_0 is similar to D_I but involves the summation over all involved excited states. Along the hole motion on the ground state, the interaction of this hole with the probe pulse may induce the transitions from the ground state to different excited states. This defines the window function W_0 . In this sense, BOMD can be used to compute the GSB signals.

Both SE and ESA signals reflect the excited-state molecular (wavepacket) motion. After the wavepacket jumps back to the ground state owing to internal conversion, the SE and ESA signals vanish, while the so-called hot GSB signal appears. Therefore, three signals (SE, ESA, and hot GSB) share the same doorway function D_I , which describes excitation from the ground electronic state to a particular excited state driven by the pump pulse.

For the SE signals, the window function W_I describes the field-matter interaction caused by the probe laser pulse during the system evolving on an excited state. The doorway and window functions are obtained at the time zero and the chosen time delay τ , respectively. The combination of them gives the SE signals.

In the calculations of the ESA signals, the window function W_{II} is determined by the electronic transitions to the high-lying excited states from the low-lying excited state on which the system is moving. This term is governed by the relevant transition energies, the corresponding TDMs, and the shape of the probe pulse. As the high-lying excited states must be included in this step, they were obtained from the single-point calculations at the snapshots obtained from the TSH dynamics simulations at the CAS-CI(16,14)/def2-SVPPD level with the MOLPRO package.^{105–107} Here, the employment of the CAS-CI with the larger active space is necessary, as it allows us to treat more high-energy electronic states with a reasonable computational cost. A total of fifteen electronic states were taken into account. After collecting the transition energies and TDMs

between excited states and considering the shape of the probe laser pulse, the window function W_{II} is obtained. Finally, the product of the doorway and window functions gives the ESA signals.

As different electronic methods were employed in above simulations, we wish to clarify the rationality of the current choice.

The BOMD was mainly used to simulate the small amplitude hole motion near the ground state minimum. We employed the B3LYP level here, as it works fast, provides smooth electronic wavefunctions along nuclear motion, and normally describes the ground-state potential well.

The nonadiabatic dynamics was simulated at the XMS-CASPT2 level: It is one of the most accurate electronic structure methods, which guarantees the sufficient accuracy in the simulation of the photolysis dynamics. Both SE and GSB signals were also obtained at the XMS-CASPT2 level.

In the calculations of the ESA signals, we have to employ the CAS-CI with a larger active space to obtain the high-lying states. Since the GSB and SE signals span a broad energy range (3–7 eV), it is essential to consider all possible transitions from the dynamics-relevant states ($S_1/S_2/S_3$) to high-lying excited states (S_n) within this spectral window to ensure comprehensive coverage of ESA signals. Moreover, the electronic characters of these high-lying states remain uncertain. To describe these states, we employed CAS-CI with a larger active space, ensuring a balanced treatment of multiconfigurational effects and improved reliability for high-lying excitations. As we wish to semi-quantitatively obtain the main features of ESA signals, the use of the CAS-CI method is acceptable. We admit that our choice is somewhat imbalanced, which may cause slight biases in the spectral simulations. However, we mainly focus on the SE signals and argue that the much weaker ESA signals are grasped qualitatively correctly.

III. RESULTS

A. Brief summary of the theoretical observables

The photodissociation dynamics of CH_3ONO_2 were carefully discussed in our previous work.⁴⁰ The current simulations with more trajectories give very similar results. Below, we summarize the key features of the nonadiabatic dynamics, as they are essential for the analyses of the TA-PP signals. More details are given in the [supplementary material](#).

- I. The S_3 state has a large TDM (Table S1 of the [supplementary material](#)), which is responsible for the strong absorption. The rapid nonadiabatic dynamics initiated in S_3 occurs within first 50–80 fs (see Fig. S1 of the [supplementary material](#)).
- II. At S_1-S_0 hops, some trajectories show longer $\text{CH}_3\text{O}-\text{NO}_2$ distances, some display longer $\text{CH}_3\text{ONO}-\text{O}$ distances, and some exhibit elongations of both. Still a few trajectories stay in the area of the short $\text{CH}_3\text{O}-\text{NO}_2$ distance (see Fig. S2 of the [supplementary material](#)).
- III. For some trajectories, the $\text{CH}_3\text{O}-\text{NO}_2$ bond elongation takes place in the early stage of dynamics and leads to a fast dissociation. Other trajectories show a few oscillations of the $\text{CH}_3\text{O}-\text{NO}_2$ bond lengths around their equilibrium values, while many of them move to the dissociation limit at a later stage.

IV. When the $\text{CH}_3\text{O}-\text{NO}_2$ bond gets broken, the excitation of the bending motion of the NO_2 moiety is observed (see Fig. S2 of the [supplementary material](#)).

V. At the end of the simulation, different photoproducts are obtained, including $\text{CH}_3\text{O} + \text{NO}_2$ (channel-I: 53%), $\text{CH}_3\text{O} + \text{NO} + \text{O}$ (channel-II, 40%), and $\text{CH}_3\text{ONO} + \text{O}$ (channel-III, 7%).

Two important experimental studies by Yang *et al.*^{22,25} and Derro *et al.*^{22,25} focused on the CH_3ONO_2 photolysis. Both suggested that the 193 nm excitation brings the system to the S_4 state. In this situation, the ratio of the $\text{CH}_3\text{ONO} + \text{O}$ channel (channel-III) is close to 30%. In the remaining 70% of products exhibiting the $\text{CH}_3\text{O}-\text{NO}_2$ bond breaking, the major energy releases to the NO_2 moiety. Yang *et al.* observed the bimodal distributions.²⁵ The low-energy part corresponded to the formation of the stable NO_2 compound, while the high-energy channel generated significantly excited NO_2 , which further dissociated into $\text{NO} + \text{O}$. Derro *et al.* suggested that the stable NO_2 compound is formed due to the excitation to the S_3 state and assumed that all dynamics from the S_4 state finally gives the $\text{CH}_3\text{O} + \text{NO} + \text{O}$ products.²² It is thus appropriate to discuss our simulations in the light of these experimental results.

First, our simulations are performed under totally different conditions. In both experiments, methyl nitrate is excited to the S_4 state, while the nonadiabatic dynamics in our simulations starts from S_3 . The experiments are performed under steady-state conditions (no time resolution) and employ narrowband lasers, while our simulations grasp the initial (~120 fs) stage of the process.

However, our simulations do provide qualitative understanding of the photolysis dynamics at higher excitation energies. We also observed that the CO bond in the CH_3O fragment is not significantly excited; see Fig. S3 of the [supplementary material](#). This indicates that energy is primarily released into the NO_2 fragment, consistent with the experimental observations. Our simulations show that the $\text{CH}_3\text{O} + \text{NO} + \text{O}$ channel plays an important role in the dynamics from S_3 . This confirms that the initial energy has to be higher than the opening threshold of this channel. Our previous calculations clearly show that the ratio of this channel quickly rises when the excitation energy is above the threshold value.⁴⁰ This confirms that higher excitation energies increase the yield of this channel. Therefore, when the dynamics starts from S_4 , we expect that the $\text{CH}_3\text{O} + \text{NO} + \text{O}$ channel becomes dominant. The same is true about the $\text{CH}_3\text{ONO} + \text{O}$ channel. Certainly, clarification of the role of the S_4 state is an open topic for the future theoretical studies.

Our work also shows that the trajectory may jump up and down in the photolysis dynamics. This indicates that the final photolysis products are formed in a more complicated manner rather than by direct mapping of the initial states of the parent compound into the final states of the photoproducts. Hence, our simulations improve the understanding of the microscopic mechanisms of the methyl nitrate photolysis.

B. Simulated TA-PP spectra and their descriptive interpretation

The TA-PP signals of CH_3ONO_2 are evaluated for the Gaussian pump and probe pulses of duration 5 fs (such pulses are available at

present in many spectroscopic labs worldwide) under assumption that the photoinduced dynamics is initiated in the state S_3 , which is achieved by the pump pulse with the carrier frequency $\omega_{pu} = 6.54$ eV. We excite to S_3 because this state is bright, possesses a high TDM, and exhibits a strong UV absorption.^{25,34,35,40}

We start our analyses from the SE contribution [Fig. 1(a)], which directly reflects the system evolution on the low-lying excited states. Initially, the maximum of the SE signal corresponds to $\omega_{pr} \approx 6.5$ eV, as expected. During the following ~ 10 fs, the signal exhibits a substantial drop of intensity. Later on, the SE signal moves to the low-energy domain, reaches a local minimum around 25 fs, exhibits a pronounced recurrence at $\sim 35\text{--}45$ fs, and vanishes afterward ~ 50 fs. We can tentatively surmise, therefore, that the nonadiabatic transition from S_3 to a lower lying state takes place on a timescale of less than ~ 50 fs, while the optically induced wavepacket motion on the coupled $S_3/S_2/S_1$ potential energy surfaces is underdamped and is governed, presumably, by a single Franck-Condon (FC) active vibrational mode.

The ESA signal is shown in Fig. 1(b). The intensity of the signal is small (see Fig. 1 caption). Yet this signal reflects the electronic transitions from the active states to the high-lying excited states at different times. The ESA signal is initiated at $\omega_{pr} \approx 4.2$ eV (the strongest contribution) as well as at $\omega_{pr} \approx 3$ and 1 eV (much weaker contributions), which reveal transitions from the initially populated state S_3 to different groups of high-lying states. Interestingly, the contributions starting at $\omega_{pr} \approx 4.2$ and 1 eV move slightly to the blue on the timescale of ~ 10 fs (which is tantamount to a slight increase in the energy gap between the low- and high-lying states involved), while the contribution around $\omega_{pr} \approx 3$ eV does not exhibit any substantial spectral shift (which corresponds to a constant energy gap). Similar to the SE signal, the ESA signal exhibits a significant drop of

intensity around 50 fs, which is a signature of the downhill nonadiabatic transition to the low-lying excited states S_1 and S_2 . Yet the ESA signal does not completely vanish after ~ 50 fs, heralding ESA from the states S_1 and S_2 . The signal is almost entirely quenched at ~ 90 fs, signaling of the CH_3ONO_2 photolysis.

The hot GSB signal is depicted in Fig. 1(c). It emerges around 30 fs, indicating the onset of the internal conversion to the electronic ground state. The hot GSB signal is quite chaotic and delocalized over ~ 5 eV in the frequency domain. This indicates that the “hot” wavepacket possesses a significant internal-conversion-induced extra energy. The hot GSB signal exhibits a significant drop in its intensity after ~ 90 fs, which is a signature of the CH_3ONO_2 dissociation. The conventional cold GSB signal is displayed in Fig. 1(d). Up to around 5 fs, the signal is quite strong, which correlates with the corresponding short-time behavior of the SE and ESA signals. At longer time, the cold GSB signal exhibits a low-amplitude oscillatory dynamics around $\omega_{pr} \approx 6.5$ eV, revealing the ground-state wavepacket motion. This is a clear signature of the non-Condon effects (cf., e.g., Ref. 108). Meanwhile, it is impossible to clearly establish a single frequency of these oscillations, presumably due to several FC-active modes contributing to the signal.

Combining all the GSB, SE, and ESA contributions, we obtain the total TA-PP signal, which is experimentally detectable. This signal is shown in Fig. 2. Clearly, the cold GSB and SE contributions dominate the total signal, while the ESA and hot GSB contributions are weak and invisible on the scale of the figure. On the contrary, the SE contribution is clearly visible, delivering the timescale of the nonadiabatic population transfer from S_3 to S_1 and S_2 and indicating a high-amplitude wavepacket motion in the excited states. This means that the information that may be extracted from the SE signals in the above discussions can also be obtained from the total

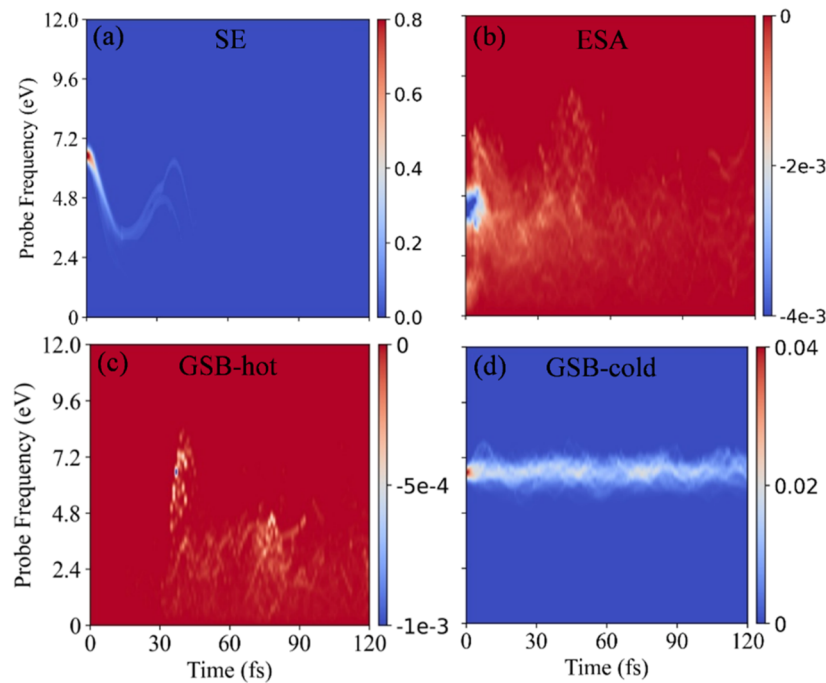


FIG. 1. Time evolution of the normalized SE (a), ESA (b), and GSB [GSB-hot (c) and GSB-cold (d)] signals calculated by the average over all trajectories. The normalization factors for the four signals are, correspondingly, 0.0445, 0.0049, 0.0012, and 0.0415.

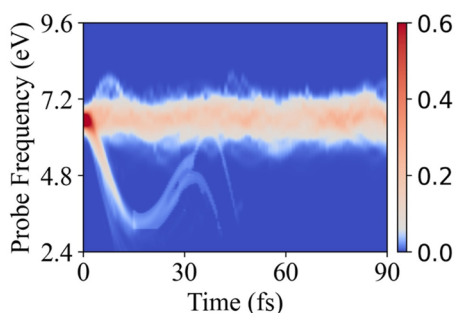


FIG. 2. Time evolution of the normalized total (SE + ESA + GSB-cold + GSB-hot) TA-PP signal. The normalization factor is 0.0445.

TA-PP signals. In this sense, the total TA-PP signal provides the clear information on the photoinduced nonadiabatic dynamics and the photolysis processes of the current system.

C. Simulation-enhanced interpretation of the TA-PP spectra

The descriptive interpretation of the TA-PP signals given in Sec. III B delivers important information on the CH_3ONO_2 photolysis. In particular, it gives us all characteristic time. In this section, we show that the interpretation can be substantially detailed, widened, and deepened by invoking the results of the electronic structure

calculations and dynamical TSH simulations of the theoretical observables summarized in Sec. III A.

We begin with the SE contributions. Two important questions should be additionally addressed in the discussion of the SE signal of Fig. 1(a). First, the SE intensity quickly weakens with time, and its decay is faster than the decay of the excited state populations in Fig. S1(b) of the [supplementary material](#). Second, the SE signal bifurcates into two branches after 20 fs and displays a pronounced recurrence around 30 fs. As explained below, all these phenomena are the fingerprints of the nonadiabatic molecular motions and directly reflect key features of different photoreaction channels.

According to Sec. III A, the initially excited S_3 state produces three photolysis channels, while channel-I ($\text{CH}_3\text{O} + \text{NO}_2$) and channel-II ($\text{CH}_3\text{O} + \text{NO} + \text{O}$) are dominant. We wish to ask whether these channels can be well monitored by the TA-PP signals, particularly SE/ESA signals. If so, the TA-PP signals provide more valuable insights to characterize the key molecular motions in the photolysis dynamics. For the SE contribution, this is shown in Fig. 3, which displays the SE signals evaluated for the two channels and four kinds of molecular motion specified in the figure caption. As shown in Figs. 3(a-1) and 3(b-1), the two channels give different SE signals. This explains the existence of two branches in the total SE signal in Fig. 1(a). Channel-II [Fig. 3(b-1)] gives stronger recurrences and higher oscillation amplitudes at 30–50 fs.

As shown in Fig. 4, both channel-I ($\text{CH}_3\text{O} + \text{NO}_2$) and channel-II ($\text{CH}_3\text{O} + \text{NO} + \text{O}$) show that many trajectories experience cleavage of the $\text{CH}_3\text{O}-\text{NO}_2$ bond. It is, therefore, worthwhile to check the

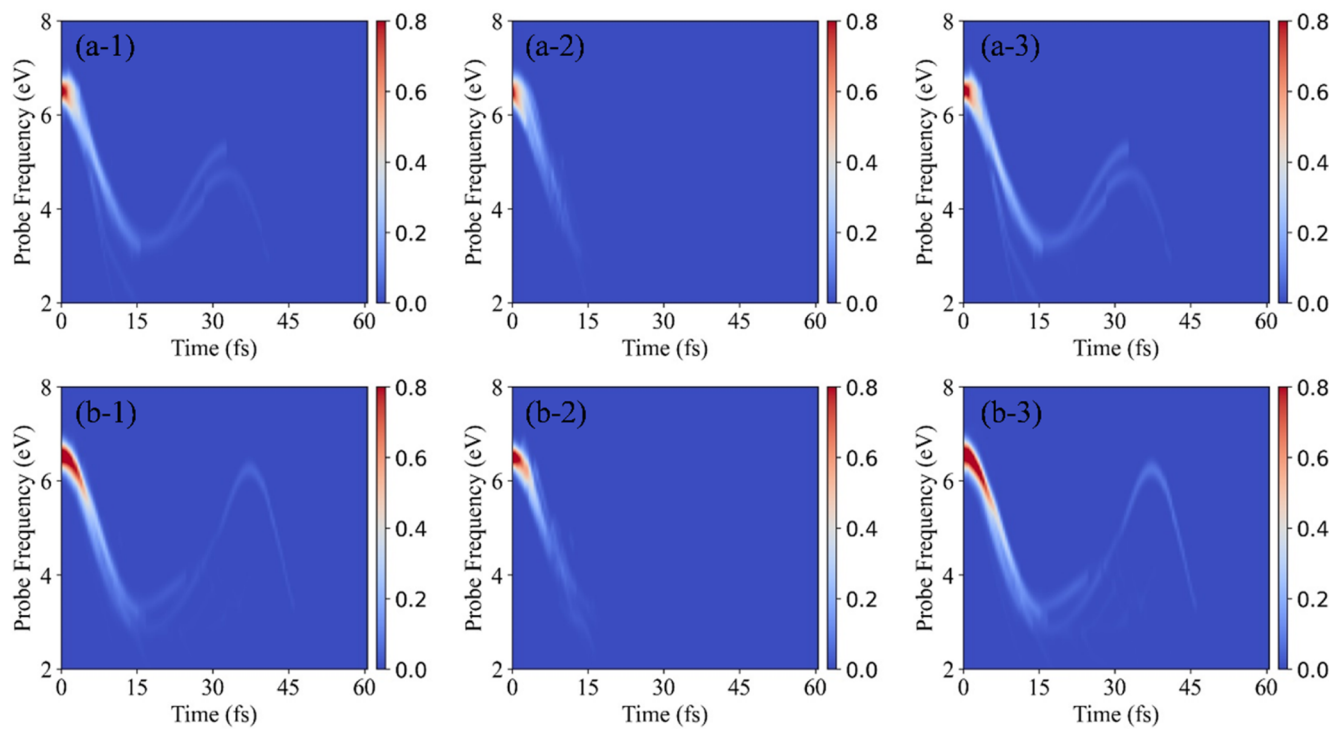


FIG. 3. Time evolution of the normalized SE signals calculated by the average over trajectories in channel-I (a-1) and channel-II (b-1), trajectories showing the $\text{CH}_3\text{O}-\text{NO}_2$ direct bond elongation in channel-I (a-2) and channel-II (b-2), and trajectories showing at least one $\text{CH}_3\text{O}-\text{NO}_2$ bond oscillation in channel-I (a-3) and channel-II (b-3).

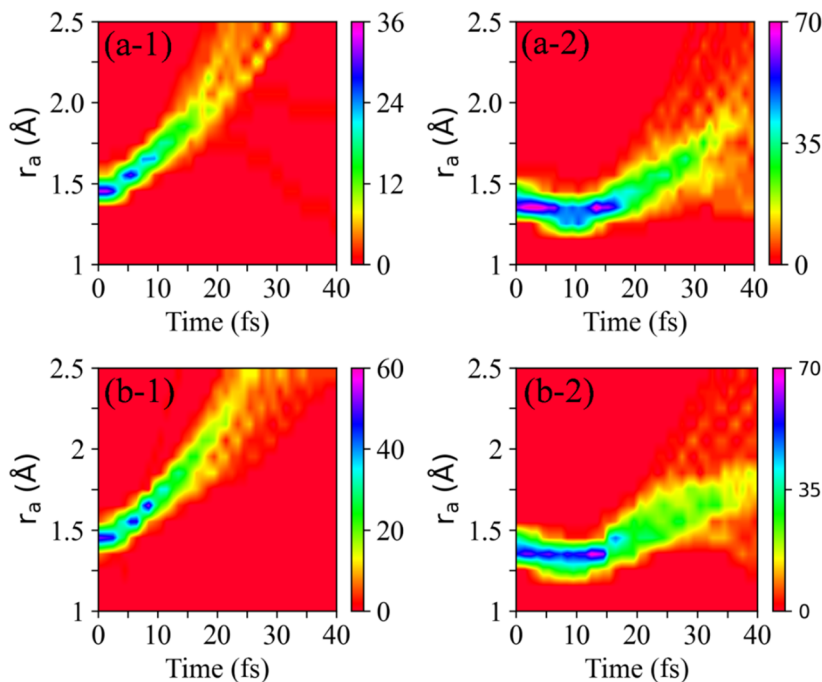


FIG. 4. Evolution of the $\text{CH}_3\text{O}-\text{NO}_2$ bond distances (r_a) for trajectories moving to channel-I [(a-1) and (a-2)] and channel-II [(b-1) and (b-2)]. The trajectories in panels (a-1) and (b-1) show the direct $\text{CH}_3\text{O}-\text{NO}_2$ bond stretch motion, while the trajectories in panels (a-2) and (b-2) exhibit at least one bond oscillation.

time-dependent evolution of the corresponding bond distances for these two channels. Interestingly, both channels include trajectories that show significant elongations of the $\text{CH}_3\text{O}-\text{NO}_2$ bond without further oscillations, leading to the direct bond breaking [panels (a-1) and (b-1) of Fig. 4]. Other trajectories in the two channels display at least a single oscillation of the $\text{CH}_3\text{O}-\text{NO}_2$ bond before 40 fs [panels (a-2) and (b-2) of Fig. 4]. Therefore, for both channels, we distinguish two types of trajectories according to whether the oscillation of the $\text{CH}_3\text{O}-\text{NO}_2$ bond appears or not. We plotted the time evolution of the $\text{CH}_3\text{O}-\text{NO}_2$ bond and the corresponding SE signals for the two types of trajectories, as shown in Figs. 3 and 4.

For channel-I ($\text{CH}_3\text{O} + \text{NO}_2$), let us first discuss the trajectories showing the direct $\text{CH}_3\text{O}-\text{NO}_2$ bond stretching and the associated SE signal. As the bond distance elongates monotonically, the system starts to break into two fragments directly. Along with this motion and the radical formation, the transition energy becomes lower and the TDM decreases dramatically, owing to the pronounced non-Condon effects. Hence, the SE signal quickly moves to the low-energy domain, as shown in Fig. 3(a-2). When the bond distance reaches 1.8 Å (see Fig. 4), the SE signal almost vanishes. Overall, the timescale of the SE quenching is highly consistent with that of the bond elongation for this group of trajectories.

The second group of trajectories in channel-I displays at least a single oscillation of the $\text{CH}_3\text{O}-\text{NO}_2$ bond. It is important to notice that this bond becomes first shorter and then longer in the early stage of the dynamics. This bond oscillation pattern clearly reflects the oscillations of the SE signal [see Fig. 3(a-3)]. At the same time, the O-N-O angle of the NO_2 moiety also shows the pronounced bending motion; see Fig. S4 of the [supplementary material](#). Then, with the further elongation of the $\text{CH}_3\text{O}-\text{NO}_2$ bond, the SE signal tends to vanish in the later stage.

Channel-II ($\text{CH}_3\text{O} + \text{NO} + \text{O}$) also includes some trajectories showing the direct $\text{CH}_3\text{O}-\text{NO}_2$ bond breaking (see Fig. 4). In fact, the further cleavage of the N-O bond of the NO_2 moiety may take place in the later stage. For these trajectories, the SE signal also moves to the low-energy domain and quickly vanishes, similar to the case of the first type of trajectories in channel-I [see Fig. 3(b-2)].

For the second type of trajectories in channel-II showing the oscillatory patterns, we also find that the $\text{CH}_3\text{O}-\text{NO}_2$ bond shortens in the early stage of the dynamics and the SE exhibits similar oscillatory features, as shown in Fig. 3(b-3). In the present case, however, some trajectories may go back to the regions that have geometries akin to the initial ones. This is proven by the typical geometries, which make a large contribution to the SE signal at 15 and 30 fs; see Fig. S3. Therefore, the recurrence of this SE signal at 30–50 fs becomes more pronounced in comparison with the SE signal produced by the second type of trajectories in channel-I.

Overall, the fast photolysis causes the SE signal to vanish earlier than the S_3 population. In fact, we often see that the TDMs of realistic systems depend strongly on the molecular motion, owing to pronounced non-Condon effects.^{67,68,93,94} If TDMs decrease significantly along the excited state wavepacket motion, the SE signal is quenched faster than the excited state populations.

The ESA signal in Fig. 1(b) is also governed by the time evolution of the nonadiabatic wavepacket in the coupled low-lying states $\text{S}_1, \text{S}_2, \text{S}_3$ and their branching into channels I and II (Fig. S5). Hence, the ESA signal can be analyzed in much the same manner as the SE signal. For example, trajectories of the first type lead to the direct dissociation in both channels, and the corresponding ESA signals also vanish very quickly, much faster than the SE signals for trajectories of the second type, as shown in Fig. S3 of the [supplementary material](#). Furthermore, a strong delocalization of the ESA spectrum

along ω_{pr} is caused by a strong dependence of the relevant TDMs on the nuclear coordinates (non-Condon effects) and pronounced bond elongation/shrinking en route to $\text{CH}_3\text{O}-\text{NO}_2$ dissociation. In addition, electronic structure calculations permit us to pinpoint the ESA signal to specific high-lying electronic states. Namely, the initial ESA spectrum centered at $\omega_{\text{pr}} \approx 4.2$ eV [Fig. 1(b)] reveals transitions from S_3 to S_{11} and S_{12} . When the wavepacket evolves on the low-lying states S_1 and S_2 , relatively weak transitions to the high-lying states become possible, which include $S_1 \rightarrow S_{6,9}$ and $S_2 \rightarrow S_{6,7,12}$ transitions.

The onset of the hot GSB signal at ~ 30 fs [Fig. 1(c)] is a signature of the $S_1 \rightarrow S_0$ internal conversion and correlates with the occurrence of the S_0 population [cf. Fig. 1(b)]. Interestingly, the hot GSB signal spreads over a broad energy domain and has a high intensity at ~ 6.5 eV within 30–40 fs. The dynamics simulations explain it as follows. After the internal conversion, some trajectories move to the FC region, in which TDMs to the low-lying excited states are high, hence resulting in broad absorption and a high intensity of the spectrum at ~ 6.5 eV, close to the $S_0 \rightarrow S_3$ transition. Later on, the trajectories move away from the FC region, and the intensity of the hot GSB signal decreases. As for the cold (lest interesting) GSB signal of Fig. 1(d), the theoretical observables add nothing profound to our understanding.

IV. CONCLUSION

We uncovered correlations between the nonadiabatic dynamics and TA-PP spectra of CH_3ONO_2 initialized in the bright state S_3 by using on-the-fly simulations. The TA-PP spectra were calculated by interfacing the TSH methodology with the classical DW simulation protocol. The photolysis mechanisms of CH_3ONO_2 were scrutinized by the combined analyses of theoretical observables (evolutions of electronic populations, bond lengths, and bond angles) and experimental observables (TA-PP spectra).

The established correspondence between the theoretical and spectroscopic observables permitted us to comprehensively characterize photoinduced nonadiabatic processes and pathways in CH_3ONO_2 , which include two major ones, channel-I ($\text{CH}_3\text{O} + \text{NO}_2$) and channel-II ($\text{CH}_3\text{O} + \text{NO} + \text{O}$), and a minor one, channel-III ($\text{CH}_3\text{ONO} + \text{O}$). Inspection of the TA-PP spectra alone allowed us to uncover characteristic timescales and qualitative features of the CH_3ONO_2 evolution of route to photofragmentation. In addition, invoking theoretical observables helped us pinpoint microscopic origins of the transformations of the TA-PP signals in the time and frequency domains. For example, quenching of the SE and ESA contributions was attributed to a high TDM of the S_3 state in comparison with the TDMs of S_2 and S_1 states and to pronounced non-Condon effects. The spectral shift, bifurcation, and temporal recurrence in the SE signal are all fully explained by the existence of the two channels and peculiarities of the nuclear motions in the channels. The spectral shift indicates that the wavepacket moves to the lowest excited state and reaches the conical intersection. The recurrence in the SE signal is attributed to the return of some trajectories to the Franck–Condon region. The SE bifurcation indicates that the low-energy and high-energy branches of the signal correspond to the $\text{CH}_3\text{O} + \text{NO}_2$ and $\text{CH}_3\text{O} + \text{NO} + \text{O}$ channels, respectively.

We conclude that the TA-PP spectrum, especially its SE contribution, captures the essentials of the nonadiabatic wavepacket motion in CH_3ONO_2 and contains valuable information on different photolysis channels. Crucially, the SE contribution is clearly visible in the total experimentally measurable TA-PP signal. We argue, therefore, that TA-PP signals will reveal fingerprints and mechanisms of the photolysis dynamics in alkyl nitrates and their derivatives, and combined *ab initio* simulations of theoretical and experimental observables will facilitate us to pinpoint microscopic origins of these mechanisms. We hope that our finding may trigger experimental explorations of methyl nitrates by the tools of femtosecond spectroscopy.

SUPPLEMENTARY MATERIAL

The [supplementary material](#) encompasses the following: the nonadiabatic dynamics simulation details, discussion on nonadiabatic dynamics, the optimized geometry of S_0 -min, the time evolution of population and key active coordinates, the electronic characters of three lowest excited states, the SE signals of channel-I and channel-II and their typical geometries at different time, the ESA signals of different types of trajectories in channel-I and channel-II, and the time-dependence of the CH_3-ONO_2 bond distances.

ACKNOWLEDGMENTS

This work was supported by NSFC projects (Grant Nos. 22333003, 22361132528, 21933011, and 22373028) and the Opening Project of Key Laboratory of Optoelectronic Chemical Materials and Devices of Ministry of Education, Jianghan University. The authors acknowledge the Supercomputing Center, Computer Network Information Center, Chinese Academy of Sciences, and the National Supercomputing Center in SunRising-1 for providing computational resources.

AUTHOR DECLARATIONS

Conflict of Interest

The authors have no conflicts to disclose.

Author Contributions

Juanjuan Zhang: Formal analysis (equal); Investigation (equal); Methodology (equal); Writing – original draft (equal); Writing – review & editing (equal). **Deping Hu:** Methodology (equal); Software (equal); Supervision (equal); Writing – review & editing (equal). **Jiawei Peng:** Data curation (equal); Investigation (equal); Supervision (equal); Writing – review & editing (equal). **Maxim F. Gelin:** Conceptualization (equal); Formal analysis (equal); Funding acquisition (equal); Writing – review & editing (equal). **Zhenggang Lan:** Conceptualization (equal); Formal analysis (equal); Funding acquisition (equal); Supervision (equal); Writing – review & editing (equal).

DATA AVAILABILITY

The data that support the findings of this study are available from the corresponding authors upon reasonable request.

REFERENCES

- ¹A. R. Ravishankara, Y. Rudich, and J. A. Pyle, "Role of chemistry in Earth's climate," *Chem. Rev.* **115**(10), 3679–3681 (2015).
- ²A. E. Perring, S. E. Pusede, and R. C. Cohen, "An observational perspective on the atmospheric impacts of alkyl and multifunctional nitrates on ozone and secondary organic aerosol," *Chem. Rev.* **113**(8), 5848–5870 (2013).
- ³T. K. Minton, C. M. Nelson, T. A. Moore, and M. Okumura, "Direct observation of ClO from chlorinating nitrate photolysis," *Science* **258**, 1342–1345 (1992).
- ⁴A. Prlj, L. M. Ibele, E. Marsili, and B. F. E. Curchod, "On the theoretical determination of photolysis properties for atmospheric volatile organic compounds," *J. Phys. Chem. Lett.* **11**(14), 5418–5425 (2020).
- ⁵I. Barnes, K. H. Becker, and T. Zhu, "Near UV absorption spectra and photolysis products of difunctional organic nitrates: Possible importance as NO_x reservoirs," *J. Atmos. Chem.* **17**, 353–373 (1993).
- ⁶X. Ruan, X. Cui, G. Jia, J. Wu, J. Zhao, D. J. Singh, Y. Liu, H. Zhang, L. Zhang, and W. Zheng, "Intramolecular heterostructured carbon nitride with heptazine-triazine for enhanced photocatalytic hydrogen evolution," *Chem. Eng. J.* **428**, 132579 (2022).
- ⁷D. Shemesh, S. A. Nizkorodov, and R. B. Gerber, "Photochemical reactions of cyclohexanone: Mechanisms and dynamics," *J. Phys. Chem. A* **120**(36), 7112–7120 (2016).
- ⁸D. Shemesh, Z. Lan, and R. B. Gerber, "Dynamics of triplet-state photochemistry of pentanal: Mechanisms of Norrish I, Norrish II, and H abstraction reactions," *J. Phys. Chem. A* **117**(46), 11711–11724 (2013).
- ⁹B. F. E. Curchod and A. J. Orr-Ewing, "Perspective on theoretical and experimental advances in atmospheric photochemistry," *J. Phys. Chem. A* **128**, 6613–6635 (2024).
- ¹⁰S. R. Utembe, L. A. Watson, D. E. Shallcross, and M. E. Jenkins, "A Common Representative Intermediates (CRI) mechanism for VOC degradation. Part 3: Development of a secondary organic aerosol module," *Atmos. Environ.* **43**(12), 1982–1990 (2009).
- ¹¹L. A. Watson, D. E. Shallcross, S. R. Utembe, and M. E. Jenkins, "A Common Representative Intermediates (CRI) mechanism for VOC degradation. Part 2: Gas phase mechanism reduction," *Atmos. Environ.* **42**(31), 7196–7204 (2008).
- ¹²M. E. Jenkins, L. A. Watson, S. R. Utembe, and D. E. Shallcross, "A Common Representative Intermediates (CRI) mechanism for VOC degradation. Part 1: Gas phase mechanism development," *Atmos. Environ.* **42**(31), 7185–7195 (2008).
- ¹³M. A. H. Khan, M. C. Cooke, S. R. Utembe, A. T. Archibald, R. G. Derwent, M. E. Jenkins, W. C. Morris, N. South, J. C. Hansen, J. S. Francisco, C. J. Percival, and D. E. Shallcross, "Global analysis of peroxy radicals and peroxy radical-water complexation using the STOCHEM-CRI global chemistry and transport model," *Atmos. Environ.* **106**, 278–287 (2015).
- ¹⁴A. Prlj, E. Marsili, L. Hutton, D. Hollas, D. Shchepanovska, D. R. Glowacki, P. Slavíček, and B. F. E. Curchod, "Calculating photoabsorption cross-sections for atmospheric volatile organic compounds," *ACS Earth Space Chem.* **6**(1), 207–217 (2022).
- ¹⁵Y. B. Lim and P. J. Ziemann, "Products and mechanism of secondary organic aerosol formation from reactions of *n*-alkanes with OH radicals in the presence of NO_x," *Environ. Sci. Technol.* **39**, 9229–9236 (2005).
- ¹⁶K. Sindelarova, C. Granier, I. Bouarar, A. Guenther, S. Tilmes, T. Stavrakou, J. F. Müller, U. Kuhn, P. Stefani, and W. Knorr, "Global data set of biogenic VOC emissions calculated by the MEGAN model over the last 30 years," *Atmos. Chem. Phys.* **14**(17), 9317–9341 (2014).
- ¹⁷S. M. Saunders, M. E. Jenkins, R. G. Derwent, and M. J. Pilling, "Protocol for the development of the master chemical mechanism, MCM v3 (Part A): Tropospheric degradation of non-aromatic volatile organic compounds," *Atmos. Chem. Phys.* **3**, 161–180 (2003).
- ¹⁸L. Vereecken and J. S. Francisco, "Theoretical studies of atmospheric reaction mechanisms in the troposphere," *Chem. Soc. Rev.* **41**(19), 6259–6293 (2012).
- ¹⁹L. M. Ibele, Y. Lassmann, T. J. Martínez, and B. F. E. Curchod, "Comparing (stochastic-selection) *ab initio* multiple spawning with trajectory surface hopping for the photodynamics of cyclopropanone, fulvene, and dithiane," *J. Chem. Phys.* **154**, 104110 (2021).
- ²⁰J. Janoš, I. S. Vinklárek, J. Rakovský, D. P. Mukhopadhyay, B. F. E. Curchod, M. Fárník, and P. Slavíček, "On the wavelength-dependent photochemistry of the atmospheric molecule CF₃COCl," *ACS Earth Space Chem.* **7**(11), 2275–2286 (2023).
- ²¹R. Atkinson, W. P. L. Carter, and A. M. Winer, "Effects of temperature and pressure on alkyl nitrate yields in the nitrogen oxide (NO_x) photooxidations of *n*-pentane and *n*-heptane," *J. Phys. Chem.* **87**(11), 2012–2018 (1983).
- ²²E. L. Derro, C. Murray, M. I. Lester, and M. D. Marshall, "Photodissociation dynamics of methyl nitrate at 193 nm: Energy disposal in methoxy and nitrogen dioxide products," *Phys. Chem. Chem. Phys.* **9**, 262–271 (2007).
- ²³W. D. Taylor, T. D. Allston, M. J. Moscato, G. B. Fazekas, R. Kozlowski, and G. A. Takacs, "Atmospheric photodissociation lifetimes for nitromethane, methyl nitrite, and methyl nitrate," *Int. J. Chem. Kinet.* **12**(4), 231–240 (1980).
- ²⁴R. M. Moore and N. V. Blough, "A marine source of methyl nitrate," *Geophys. Res. Lett.* **29**, 27, <https://doi.org/10.1029/2002gl014989> (2002).
- ²⁵X. Yang, P. Felder, and J. R. Huber, "Photodissociation of methyl nitrate in a molecular beam," *J. Phys. Chem.* **97**, 10903–10910 (1993).
- ²⁶R. Atkinson, "Kinetics and mechanisms of the gas-phase reactions of the NO₃ radical with organic compounds," *J. Phys. Chem. Ref. Data* **20**, 459–507 (1991).
- ²⁷A. L. Chuck, S. M. Turner, and P. S. Liss, "Direct evidence for a marine source of C₁ and C₂ alkyl nitrates," *Science* **297**, 1151–1154 (2002).
- ²⁸M. P. Turberg, D. M. Giolando, C. Tilt, T. Soper, S. Mason, M. Davies, P. Klingensmith, and G. A. Takacs, "Atmospheric photochemistry of alkyl nitrates," *J. Photochem. Photobiol. A* **51**, 281–292 (1990).
- ²⁹D. E. Shallcross, P. Biggs, C. E. Canosa-Mas, K. C. Clemmitshaw, M. G. Harrison, M. Reyes López Alañón, J. A. Pyle, A. Vipond, and R. P. Wayne, "Rate constants for the reaction between OH and CH₃ONO₂ and C₂H₅ONO₂ over a range of pressure and temperature," *J. Chem. Soc., Faraday Trans.* **93**, 2807–2811 (1997).
- ³⁰R. K. Talukdar, J. B. Burkholder, M. Hunter, M. K. Gilles, J. M. Roberts, and A. R. Ravishankara, "Atmospheric fate of several alkyl nitrates Part 2 UV absorption cross-sections and photodissociation quantum yields," *J. Chem. Soc., Faraday Trans.* **93**, 2797–2805 (1997).
- ³¹R. K. Talukdar, S. C. Herndon, J. B. Burkholder, J. M. Roberts, and A. R. Ravishankara, "Atmospheric fate of several alkyl nitrates Part 1 Rate coefficients of the reactions of alkyl nitrates with isotopically labelled hydroxyl radicals," *J. Chem. Soc., Faraday Trans.* **93**, 2787–2796 (1997).
- ³²A. Bacak, M. W. Bardwell, M. T. Raventos, C. J. Percival, G. Sanchez-Reyna, and D. E. Shallcross, "Kinetics of the reaction of CH₃O₂ + NO: A temperature and pressure dependence study with chemical ionization mass spectrometry," *J. Phys. Chem. A* **108**, 10681–10687 (2004).
- ³³A. Lesar, M. Hodošek, E. Drougas, and A. M. Kosmas, "Quantum mechanical investigation of the atmospheric reaction CH₃O₂ + NO," *J. Phys. Chem. A* **110**, 7898–7903 (2006).
- ³⁴J. Soto, D. Peláez, J. C. Otero, F. J. Avila, and J. F. Arenas, "Photodissociation mechanism of methyl nitrate. A study with the multistate second-order multiconfigurational perturbation theory," *Phys. Chem. Chem. Phys.* **11**(15), 2631–2639 (2009).
- ³⁵P. G. Carbo and A. J. Orr-Ewing, "NO₂ quantum yields from ultraviolet photodissociation of methyl and isopropyl nitrate," *Phys. Chem. Chem. Phys.* **12**(23), 6084–6091 (2010).
- ³⁶S. He, Z. Chen, and X. Zhang, "Photochemical reactions of methyl and ethyl nitrate: A dual role for alkyl nitrates in the nitrogen cycle," *Environ. Chem.* **8**(6), 529 (2011).
- ³⁷M. Isegawa, F. Liu, S. Maeda, and K. Morokuma, "Ab initio reaction pathways for photodissociation and isomerization of nitromethane on four singlet potential energy surfaces with three roaming paths," *J. Chem. Phys.* **140**(24), 244310 (2014).
- ³⁸C. M. Higgins, L. A. Evans, G. C. Lloyd-Jones, D. E. Shallcross, D. P. Tew, and A. J. Orr-Ewing, "Quantum yields for photochemical production of NO₂ from organic nitrates at tropospherically relevant wavelengths," *J. Phys. Chem. A* **118**(15), 2756–2764 (2014).
- ³⁹J. E. Williams, G. Le Bras, A. Kukui, H. Ziereis, and C. A. M. Brenninkmeijer, "The impact of the chemical production of methyl nitrate from the NO + CH₃O₂ reaction on the global distributions of alkyl nitrates, nitrogen oxides and tropospheric ozone: A global modelling study," *Atmos. Chem. Phys.* **14**(5), 2363–2382 (2014).
- ⁴⁰J. Zhang, J. Peng, D. Hu, and Z. Lan, "Investigation of nonadiabatic dynamics in the photolysis of methyl nitrate (CH₃ONO₂) by on-the-fly surface hopping simulation," *Phys. Chem. Chem. Phys.* **23**, 25597–25611 (2021).

- ⁴¹J. Zhang, J. Peng, D. Hu, C. Xu, and Z. Lan, "Understanding photolysis of CH₃ONO₂ with on-the-fly nonadiabatic dynamics simulation at the ADC(2) level," *Chin. J. Chem. Phys.* **35**(3), 451–460 (2022).
- ⁴²J. Soto, D. Peláez, and J. C. Otero, "A SA-CASSCF and MS-CASPT2 study on the electronic structure of nitrosobenzene and its relation to its dissociation dynamics," *J. Chem. Phys.* **154**(4), 044307 (2021).
- ⁴³J. Soto, F. J. Avila, J. C. Otero, D. Peláez, and J. F. Arenas, "A molecular mechanism for direct generation of nitric oxide, peroxynitrite and superoxide in the reaction of nitroglycerin with a cysteinyl-cysteine derivative," *Theor. Chem. Acc.* **128**(4–6), 593–599 (2010).
- ⁴⁴J. M. Roberts and R. W. Fajer, "UV absorption cross sections of organic nitrates of potential atmospheric importance and estimation of atmospheric lifetimes," *Environ. Sci. Technol.* **23**(8), 945–951 (1989).
- ⁴⁵J. Zhang, J. Peng, Y. Zhu, D. Hu, and Z. Lan, "Influence of mode-specific excitation on the nonadiabatic dynamics of methyl nitrate (CH₃ONO₂)," *J. Phys. Chem. Lett.* **14**(29), 6542–6549 (2023).
- ⁴⁶J. Peng, H. Liu, and Z. Lan, "The photodissociation dynamics and ultrafast electron diffraction image of cyclobutanone from the surface hopping dynamics simulation," *J. Chem. Phys.* **160**(22), 224305 (2024).
- ⁴⁷T. J. A. Wolf, D. M. Sanchez, J. Yang, R. M. Parrish, J. P. F. Nunes, M. Centurion, R. Coffee, J. P. Cryan, M. Gühr, K. Hegazy, A. Kirrander, R. K. Li, J. Ruddock, X. Shen, T. Vecchione, S. P. Weathersby, P. M. Weber, K. Wilkin, H. Yong, Q. Zheng, X. J. Wang, M. P. Minitti, and T. J. Martínez, "The photochemical ring-opening of 1,3-cyclohexadiene imaged by ultrafast electron diffraction," *Nat. Chem.* **11**(6), 504–509 (2019).
- ⁴⁸J. Janoš, J. P. Figueira Nunes, D. Hollas, P. Slavíček, and B. F. E. Curchod, "Predicting the photodynamics of cyclobutanone triggered by a laser pulse at 200 nm and its MeV-UED signals—A trajectory surface hopping and XMS-CASPT2 perspective," *J. Chem. Phys.* **160**(14), 144305 (2024).
- ⁴⁹H. R. Hudock, B. G. Levine, A. L. Thompson, H. Satzger, D. Townsend, N. Gador, S. Ullrich, A. Stolow, and T. J. Martínez, "Ab initio molecular dynamics and time-resolved photoelectron spectroscopy of electronically excited uracil and thymine," *J. Phys. Chem. A* **111**(34), 8500–8508 (2007).
- ⁵⁰T. J. Penfold and B. F. E. Curchod, "Exploring the influence of approximations for simulating valence excited X-ray spectra," *J. Phys. Chem. A* **128**(50), 10826–10836 (2024).
- ⁵¹T. Piteša, M. Sapunar, A. Ponzi, M. F. Gelin, N. Došlić, W. Domcke, and P. Decleva, "Combined surface-hopping, dyson orbital, and B-spline approach for the computation of time-resolved photoelectron spectroscopy signals: The internal conversion in pyrazine," *J. Chem. Theory Comput.* **17**(8), 5098–5109 (2021).
- ⁵²W. Arbelo-González, R. Crespo-Otero, and M. Barbatti, "Steady and time-resolved photoelectron spectra based on nuclear ensembles," *J. Chem. Theory Comput.* **12**(10), 5037–5049 (2016).
- ⁵³C. Wang, M. D. J. Waters, P. Zhang, J. Suchan, V. Svoboda, T. T. Luu, C. Perry, Z. Yin, P. Slavíček, and H. J. Wörner, "Different timescales during ultrafast stilbene isomerization in the gas and liquid phases revealed using time-resolved photoelectron spectroscopy," *Nat. Chem.* **14**(10), 1126–1132 (2022).
- ⁵⁴V. Bonačić-Koutecký and R. Mitić, "Theoretical exploration of ultrafast dynamics in atomic clusters: Analysis and control," *Chem. Rev.* **105**(1), 11–66 (2005).
- ⁵⁵S. Pathak, L. M. Ibele, R. Boll, C. Callegari, A. Demidovich, B. Erk, R. Feifel, R. Forbes, M. Di Fraia, L. Giannessi, C. S. Hansen, D. M. P. Holland, R. A. Ingle, R. Mason, O. Plekan, K. C. Prince, A. Rouzée, R. J. Squibb, J. Tross, M. N. R. Ashfold, B. F. E. Curchod, and D. Rolles, "Tracking the ultraviolet-induced photochemistry of thiophene during and after ultrafast ring opening," *Nat. Chem.* **12**(9), 795–800 (2020).
- ⁵⁶A. Tortschanoff and S. Mukamel, "Pump–probe simulation study of the two-exciton manifold of dendrimers," *J. Phys. Chem. A* **106**, 7521–7529 (2002).
- ⁵⁷A. Mehmood, M. C. Silfies, A. S. Durden, T. K. Allison, and B. G. Levine, "Simulating ultrafast transient absorption spectra from first principles using a time-dependent configuration interaction probe," *J. Chem. Phys.* **161**(4), 044107 (2024).
- ⁵⁸Y. Bai, W. Ni, K. Sun, L. Chen, L. Ma, Y. Zhao, G. G. Gurzadyan, and M. F. Gelin, "Plenty of room on the top: Pathways and spectroscopic signatures of singlet fission from upper singlet states," *J. Phys. Chem. Lett.* **13**(48), 11086–11094 (2022).
- ⁵⁹M. Maiuri, M. Garavelli, and G. Cerullo, "Ultrafast spectroscopy: State of the art and open challenges," *J. Am. Chem. Soc.* **142**(1), 3–15 (2020).
- ⁶⁰W. M. Zhang, V. Chernyak, and S. Mukamel, "Multidimensional femtosecond correlation spectroscopies of electronic and vibrational excitons," *J. Chem. Phys.* **110**, 5011–5028 (1999).
- ⁶¹M. Kowalewski, B. P. Fingerhut, K. E. Dorfman, K. Bennett, and S. Mukamel, "Simulating coherent multidimensional spectroscopy of nonadiabatic molecular processes: From the infrared to the X-ray regime," *Chem. Rev.* **117**, 12165–12226 (2017).
- ⁶²N. Gross, C. T. Kuhs, B. Ostovar, W.-Y. Chiang, K. S. Wilson, T. S. Volek, Z. M. Faitz, C. C. Carlin, J. A. Dionne, M. T. Zanni, M. Gruebele, S. T. Roberts, S. Link, and C. F. Landes, "Progress and prospects in optical ultrafast microscopy in the visible spectral region: Transient absorption and two-dimensional microscopy," *J. Phys. Chem. C* **127**(30), 14557–14586 (2023).
- ⁶³T. Begušić, J. Roulet, and J. Vaníček, "On-the-fly *ab initio* semiclassical evaluation of time-resolved electronic spectra," *J. Chem. Phys.* **149**, 244115 (2018).
- ⁶⁴S. Mukamel, *Principles of Nonlinear Optical Spectroscopy* (Oxford University Press, 1995).
- ⁶⁵R. Spesvtsev, J. G. Underwood, and H. H. Fielding, in *Ultrafast Phenomena in Molecular Sciences: Femtosecond Physics and Chemistry*, edited by R. Nalda and L. Bañares (Springer International Publishing, 2014).
- ⁶⁶M. F. Gelin, Z. Lan, N. Došlić, and W. Domcke, "Computation of time-resolved nonlinear electronic spectra from classical trajectories," *Wiley Interdiscip. Rev.: Comput. Mol. Sci.* **15**, e70012 (2025).
- ⁶⁷A. E. Boguslavskiy, O. Schalk, N. Gador, W. J. Glover, T. Mori, T. Schultz, M. S. Schuurman, T. J. Martinez, and A. Stolow, "Excited state non-adiabatic dynamics of the smallest polyene, trans 1,3-butadiene. I. Time-resolved photoelectron-photoion coincidence spectroscopy," *J. Chem. Phys.* **148**(16), 164302 (2018).
- ⁶⁸M. Williams, R. Forbes, H. Weir, K. Veyrinas, R. J. MacDonell, A. E. Boguslavskiy, M. S. Schuurman, A. Stolow, and T. J. Martinez, "Unmasking the cis-stilbene phantom state via vacuum ultraviolet time-resolved photoelectron spectroscopy and ab initio multiple spawning," *J. Phys. Chem. Lett.* **12**(27), 6363–6369 (2021).
- ⁶⁹W. T. Pollard, S. Y. Lee, and R. A. Mathies, "Wave packet theory of dynamic absorption spectra in femtosecond pump–probe experiments," *J. Chem. Phys.* **92**(7), 4012–4029 (1990).
- ⁷⁰W. T. Pollard and R. A. Mathies, "Analysis of femtosecond dynamic absorption spectra of nonstationary states," *Annu. Rev. Phys. Chem.* **43**(1), 497–523 (1992).
- ⁷¹Y. J. Yan and S. Mukamel, "Femtosecond pump–probe spectroscopy of polyatomic molecules in condensed phases," *Phys. Rev. A* **41**, 6485–6504 (1990).
- ⁷²Y. J. Yan, L. E. Fried, and S. Mukamel, "Ultrafast pump–probe spectroscopy: Femtosecond dynamics in Liouville space," *J. Phys. Chem.* **93**(25), 8149–8162 (1989).
- ⁷³G. Stock, "Classical description of nonadiabatic photoisomerization processes and their real-time detection via femtosecond spectroscopy," *J. Chem. Phys.* **103**(23), 10015–10029 (1995).
- ⁷⁴Z. Li, J. Y. Fang, and C. C. Martens, "Simulation of ultrafast dynamics and pump–probe spectroscopy using classical trajectories," *J. Chem. Phys.* **104**(18), 6919–6929 (1996).
- ⁷⁵L. W. Ungar and J. A. Cina, "Short-time fluorescence Stokes shift dynamics," *Adv. Chem. Phys.* **100**, 171–228 (1997).
- ⁷⁶S. A. Pentidis and R. F. Loring, "Calculation of the photon echo with mixed-state propagation," *Chem. Phys. Lett.* **287**(3–4), 217–223 (1998).
- ⁷⁷S. M. Gruenbaum and R. F. Loring, "Semiclassical mean-trajectory approximation for nonlinear spectroscopic response functions," *J. Chem. Phys.* **129**(12), 124510 (2008).
- ⁷⁸I. Conti, G. Cerullo, A. Nenov, and M. Garavelli, "Ultrafast spectroscopy of photoactive molecular systems from first principles: Where we stand today and where we are going," *J. Am. Chem. Soc.* **142**(38), 16117–16139 (2020).
- ⁷⁹D. Avagliano, M. Bonfanti, A. Nenov, and M. Garavelli, "Automatized protocol and interface to simulate QM/MM time-resolved transient absorption at TD-DFT level with COBRAMM," *J. Comput. Chem.* **43**(24), 1641–1655 (2022).
- ⁸⁰T. Begušić and J. Vaníček, "On-the-fly *ab initio* semiclassical evaluation of third-order response functions for two-dimensional electronic spectroscopy," *J. Chem. Phys.* **153**, 184110 (2020).

- ⁸¹F. P. Bonafé, F. J. Hernández, B. Aradi, T. Frauenheim, and C. G. Sánchez, "Fully atomistic real-time simulations of transient absorption spectroscopy," *J. Phys. Chem. Lett.* **9**(15), 4355–4359 (2018).
- ⁸²F. P. Bonafé, B. Aradi, B. Hourahine, C. R. Medrano, F. J. Hernández, T. Frauenheim, and C. G. Sánchez, "A real-time time-dependent density functional tight-binding implementation for semiclassical excited state electron-nuclear dynamics and pump-probe spectroscopy simulations," *J. Chem. Theory Comput.* **16**, 4454–4469 (2020).
- ⁸³J. Krumland, A. M. Valencia, S. Pittalis, C. A. Rozzi, and C. Cocchi, "Understanding real-time time-dependent density-functional theory simulations of ultrafast laser-induced dynamics in organic molecules," *J. Chem. Phys.* **153**(5), 054106 (2020).
- ⁸⁴J. Segarra-Martí, S. Mukamel, M. Garavelli, A. Nenov, and I. Rivalta, "Towards accurate simulation of two-dimensional electronic spectroscopy," *Top. Curr. Chem.* **376**(3), 24 (2018).
- ⁸⁵R. Borrego-Varillas, A. Nenov, P. Kabaciński, I. Conti, L. Ganzer, A. Oriana, V. K. Jaiswal, I. Delfino, O. Weingart, C. Manzoni, I. Rivalta, M. Garavelli, and G. Cerullo, "Tracking excited state decay mechanisms of pyrimidine nucleosides in real time," *Nat. Commun.* **12**(1), 7285 (2021).
- ⁸⁶X. Huang, W. Xie, N. Došlić, M. F. Gelin, and W. Domcke, "Ab initio quasiclassical simulation of femtosecond time-resolved two-dimensional electronic spectra of pyrazine," *J. Phys. Chem. Lett.* **12**, 11736–11744 (2021).
- ⁸⁷M. F. Gelin, X. Huang, W. Xie, L. Chen, N. Došlić, and W. Domcke, "Ab initio surface-hopping simulation of femtosecond transient-absorption pump-probe signals of nonadiabatic excited-state dynamics using the doorway-window representation," *J. Chem. Theory Comput.* **17**, 2394–2408 (2021).
- ⁸⁸M. F. Gelin, L. Chen, and W. Domcke, "Equation-of-motion methods for the calculation of femtosecond time-resolved 4-wave-mixing and *N*-wave-mixing signals," *Chem. Rev.* **122**, 17339–17396 (2022).
- ⁸⁹S. L. Horton, Y. Liu, P. Chakraborty, P. Marquetand, T. Rozgonyi, S. Matsika, and T. Weinacht, "Strong-field- versus weak-field-ionization pump-probe spectroscopy," *Phys. Rev. A* **98**(5), 053416 (2018).
- ⁹⁰B. J. Ka and E. Geva, "A nonperturbative calculation of nonlinear spectroscopic signals in liquid solution," *J. Chem. Phys.* **125**(21), 214501 (2006).
- ⁹¹F. Martinez and G. Hanna, "Mixed quantum-classical simulations of transient absorption pump-probe signals for a photo-induced electron transfer reaction coupled to an inner-sphere vibrational mode," *J. Phys. Chem. A* **120**(19), 3196–3205 (2016).
- ⁹²X. Gao and E. Geva, "A nonperturbative methodology for simulating multidimensional spectra of multie excitonic molecular systems via quasiclassical mapping Hamiltonian methods," *J. Chem. Theory Comput.* **16**(10), 6491–6502 (2020).
- ⁹³C. Xu, K. Lin, D. Hu, F. L. Gu, M. F. Gelin, and Z. Lan, "Ultrafast internal conversion dynamics through the on-the-fly simulation of transient absorption pump-probe spectra with different electronic structure methods," *J. Phys. Chem. Lett.* **13**(2), 661–668 (2022).
- ⁹⁴D. Hu, J. Peng, L. Chen, M. F. Gelin, and Z. Lan, "Spectral fingerprint of excited-state energy transfer in dendrimers through polarization-sensitive transient-absorption pump-probe signals: On-the-fly nonadiabatic dynamics simulations," *J. Phys. Chem. Lett.* **12**, 9710–9719 (2021).
- ⁹⁵C. Xu, C. Lin, J. Peng, J. Zhang, S. Lin, F. L. Gu, M. F. Gelin, and Z. Lan, "On-the-fly simulation of time-resolved fluorescence spectra and anisotropy," *J. Chem. Phys.* **160**(10), 104109 (2024).
- ⁹⁶P. Chakraborty, Y. Liu, S. McClung, T. Weinacht, and S. Matsika, "Time resolved photoelectron spectroscopy as a test of electronic structure and nonadiabatic dynamics," *J. Phys. Chem. Lett.* **12**, 5099–5104 (2021).
- ⁹⁷P. Chakraborty and S. Matsika, "Time-resolved photoelectron spectroscopy via trajectory surface hopping," *WIREs Comput. Mol. Sci.* **14**(3), e1715 (2024).
- ⁹⁸J. Finley, P.-Å. Malmqvist, B. O. Roos, and L. Serrano-Andrés, "The multi-state CASPT2 method," *Chem. Phys. Lett.* **288**, 299–306 (1998).
- ⁹⁹A. A. Granovsky, "Extended multi-configuration quasi-degenerate perturbation theory: The new approach to multi-state multi-reference perturbation theory," *J. Chem. Phys.* **134**(21), 214113 (2011).
- ¹⁰⁰T. Shiozaki, W. Győrffy, P. Celani, and H. J. Werner, "Communication: Extended multi-state complete active space second-order perturbation theory: Energy and nuclear gradients," *J. Chem. Phys.* **135**(8), 081106 (2011).
- ¹⁰¹L. Du and Z. Lan, "An on-the-fly surface-hopping program JADE for nonadiabatic molecular dynamics of polyatomic systems: Implementation and applications," *J. Chem. Theory Comput.* **11**, 1360–1374 (2015).
- ¹⁰²D. Hu, Y. F. Liu, A. L. Sobolewski, and Z. Lan, "Nonadiabatic dynamics simulation of keto isocytosine: A comparison of dynamical performance of different electronic-structure methods," *Phys. Chem. Chem. Phys.* **19**(29), 19168–19177 (2017).
- ¹⁰³D. Hu, Y. Xie, J. Peng, and Z. Lan, "On-the-fly symmetrical quasi-classical dynamics with Meyer-Miller mapping Hamiltonian for the treatment of nonadiabatic dynamics at conical intersections," *J. Chem. Theory Comput.* **17**, 3267–3279 (2021).
- ¹⁰⁴S. Grimme, S. Ehrlich, and L. Goerigk, "Effect of the damping function in dispersion corrected density functional theory," *J. Comput. Chem.* **32**(7), 1456–1465 (2011).
- ¹⁰⁵H.-J. Werner, P. J. Knowles, G. Knizia, F. R. Manby, and M. Schütz, "Molpro: A general-purpose quantum chemistry program package," *WIREs Comput. Mol. Sci.* **2**(2), 242–253 (2012).
- ¹⁰⁶Q. Ma and H.-J. Werner, "Explicitly correlated local coupled-cluster methods using pair natural orbitals," *WIREs Comput. Mol. Sci.* **8**(6), e1371 (2018).
- ¹⁰⁷H.-J. Werner, P. J. Knowles, F. R. Manby, J. A. Black, K. Doll, A. Hefelmann, D. Kats, A. Köhn, T. Korona, D. A. Kreplin, Q. Ma, T. F. Miller III, A. Mitrushchenkov, K. A. Peterson, I. Polyak, G. Rauhut, and M. Sibaev, "The Molpro quantum chemistry package," *J. Chem. Phys.* **152**(14), 144107 (2020).
- ¹⁰⁸G. Granucci and M. Persico, "Critical appraisal of the fewest switches algorithm for surface hopping," *J. Chem. Phys.* **126**, 134114 (2007).